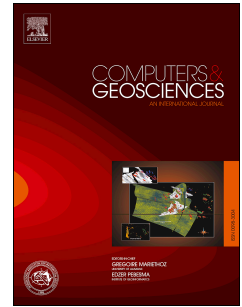# Accepted Manuscript

Automated high accuracy, rapid beam hardening correction in X-ray computed tomography of multi-mineral, heterogeneous core samples

Carla Romano, James M. Minto, Zoe K. Shipton, Rebecca J. Lunn

Please cite this article as: Romano, C., Minto, J.M., Shipton, Z.K., Lunn, R.J., Automated high accuracy, rapid beam hardening correction in X-ray computed tomography of multi-mineral, heterogeneous core samples, *Computers and Geosciences* (2019), doi: https://doi.org/10.1016/j.cageo.2019.06.009.

1 **Automated high accuracy, rapid beam hardening correction in X-Ray Computed**
2 **Tomography of multi-mineral, heterogeneous core samples**

3 Carla Romano[1], James M. Minto, Zoe K. Shipton and Rebecca J. Lunn

4 *Department of Civil and Environmental Engineering, University of Strathclyde, Glasgow, UK*

5 Corresponding author: Carla Romano (carla.romano@strath.ac.uk)
6 Permanent address: 75 Montrose Street, James Weir Building, Level 5, Glasgow, G1 1XJ

7 Link to code: http://dx.doi.org/10.15129/2fb54088-1187-48f2-832b-ef76cf5e7bc1

8 **Authorship statement**

9 1. Carla Romano: acquired CT data, wrote the manuscript and the code, and acted as
10   corresponding author;
11 2. James M. Minto: acquired CT data, edited the manuscript and the code
12 3. Zoe K. Shipton: edited the manuscript and supervised development of the research
13 4. Rebecca J. Lunn: edited the manuscript and supervised development of the research

14 **Highlights**

15 • We introduce a new and automatic method for correcting CT beam hardening artefact
16 • The method is implemented in an open source code running in ImageJ and it is suitable
17   for expert and non-expert alike.
18 • The method has been tested on homogeneous and heterogeneous rock samples with
19   cylindrical and near-cylindrical shapes
20 • We show how our method improves porosity and permeability measurements.

21

[1] Present address (Visiting Researcher Student): Department of Energy Resources Engineering, Green Earth Science Building, 367 Panama Mall, Stanford, California 94305

22 **Abstract**

23 X-ray Computed Tomography scanning is an innovative procedure that allows representing the
24 internal structure of samples. Among its several purposes, X-ray CT is widely used for
25 investigation of petrophysical properties of porous media. To provide accurate results, it is
26 necessary to have high quality scan images, free of artefacts. One of the most problematic
27 artefacts is beam hardening, which, in cylindrical shapes, increases the attenuation values with
28 increasing distance from the centre. Until now, no automatic solution has been proposed for
29 cylindrically-shaped cores that is both computationally feasible and applicable to all geological
30 media. A new technique is here introduced for correcting beam hardening, using a linearization
31 procedure of the beam hardening curve applied after the reconstruction process. We have
32 developed an automated open source plug-in, running on ImageJ software, which does not
33 require any *a priori* knowledge of the material, distance from the source or the scan conditions
34 (current, energy), nor any segmentation of phases or calibration scan on phantom data. It is
35 suitable for expert and non-expert use, alike. We have tested the technique on μCT scan images
36 of a plastic rod, a sample of loose sand, several heterogeneous sandstone core samples (with
37 near-cylindrical shapes), and finally, on an internal scan of a Berea sandstone core. The Berea
38 core was also scanned using a medical X-ray CT scanner with a fan-beam geometry, as opposed
39 to a cone beam geometry, showing that our algorithm is equally effective in both cases. Our
40 correction technique successfully removes the beam hardening artefact in all cases, as well as
41 removing the cupping effect common to internal scans. For a Berea Sandstone, which varies in
42 porosity from 19%-20%, porosity calculated using the corrected scan is 20.54%, which compares
43 to a value of 14.24% using the software provided by the manufacturer.

44 **Key Points:**

45 • Computed Tomography

46 • Beam hardening

47 • Image Analysis

48 • Geology

49 • Petrophysics

1 Introduction

X-ray Computed Tomography (X-ray CT) is a modern non-intrusive imaging technique that produces cross-sectional images (*slices*) of a sample and, using tomography, allows three-dimensional reconstruction of the sample. X- ray CT is widely used in life science, and in the last 30 years, it has completely revolutionized measurement techniques in geoscience. Early X-ray analysis was mostly applied to paleontology and petroleum engineering (Wellington & Vinegar, 1987). In recent years, thanks to technological progress, and the possibility to reach micrometer resolution, it boasts many more geological applications. For example, it has been used to measure macroscopic soil porosity (Mooney, 2002), pore structure of hydrocarbon reservoir rocks (Van Geet, et al., 2000), and for visualisation of roots in soil (Mooney, et al., 2012). X-ray CT has been integrated into core flooding experiments for understanding how to enhance oil recovery in oil-brine systems (Lager, et al., 2008), and to illuminate trapping mechanisms for carbon storage (Perrin, et al., 2009). Moreover, X-ray CT allows the production of 3D porosity distributions and spatial and temporal measurement of saturation distribution of each phase during multiphase flow experiments. To ensure accurate quantitative results, it is necessary to have high quality images that avoid sources of error, such as artefacts due to the reconstruction process.

A beam of X-rays passes through the sample and radiation is measured by a detection system (*detector*) to produce attenuation profiles. The attenuation values are related to the electron densities of the sample's components (Kruth, et al., 2011) and the energy and current values of the scan. All the instruments are characterized by a source-sample-detector system, but in relation to the geometries of the source (point or linear source) and the detector (linear or planar), there are different beam shapes. Cone beam geometry X-ray CT scanners are characterized by a fixed-point X-ray source and a planar detector. The beam is cone shaped and each ray passes through the object with a certain angle. This enables higher resolution images (Lechuga & Weidlich, 2016) but results in a more complicated reconstruction process. In fan beam geometry, instead, the source is a point source and the detector is a curved array. The beam is planar fan shaped and the incident rays are perpendicular to the object. In this case, the reconstruction is fast, but the resolution is low. Artefacts and limitations are mainly related to the operator choices and the reconstruction (Cnudde & Boone, 2013). Such artefacts may affect the accuracy of the measurements of interest. One of the most common artefacts is so-called beam hardening, derived from the incorrect assumption of a monochromatic source, whereas most of the X-ray systems are characterized by polychromatic sources. This assumption is made by the most commonly used and fast method for three-dimensional reconstruction, i.e. Filtered Back Projection (Feldkamp, et al., 1984).

A monochromatic source produces waves with same wavelength. In this case the X-ray is uniformly attenuated when it passes through the sample and the attenuation depends on the X-ray energy and the sample's composition, in accordance with the Beer's Law:

$$I = I_0\, e^{-\int \mu(s)ds} \qquad (1)$$

where I is the X-ray intensity, μ is the attenuation, and s is the ray path (Cnudde & Boone, 2013). A polychromatic source, instead, produces radiations with more than one wavelength; the

90 components of the spectra are not uniformly attenuated, and the lower energies are absorbed
91 more easily by the sample. The consequence of assuming a monochromatic source in the
92 reconstruction process is often higher attenuation values at the sample edges than the centre. This
93 artefact is often termed a cupping effect. Because the measurement of petrophysical properties
94 (i.e. porosity, relative permeability, capillarity) are strictly related to the quality of the X-Ray
95 images, ignoring the beam hardening artefact effects their accuracy.

96 Different approaches have been proposed to correct the beam hardening artefact, but no solutions
97 that are computationally possible on large datasets, and applicable to all types of materials, have
98 yet been developed. Using physical filters (Jennings, 1988) before scanning often requires higher
99 exposure and it can be time demanding and not economically sustainable. In addition, multiple
100 trials are necessary to define the best filter and the correction of the artefact is not certain. In
101 addition to Filtered Back Projection, several iterative reconstruction (ART, SART, SIRT,
102 MLEM, etc.) methods can be applied on projection data (Gilbert, 1972; Biguri, et al., 2016).
103 However, the computation of these methods on large datasets, such as the 14 GB that results
104 from 3142 projections, is not possible on a standard computer. Most of the pre-reconstruction
105 linearization methods rely on producing a calibration scan using a phantom object with the same
106 density as the sample (Kachelrieß, et al., 2006; Ritschl, et al., 2010). The method cannot be
107 applied if the sample is heterogeneous, multi-material and/or of unknown density. Consequently,
108 these methods are not suitable for correcting scans of geological samples. Linearization can be
109 also determined by pre-determined correction profiles, custom user-specified correction profiles,
110 and custom auto-detected correction profiles (such as those utilized by CT pro 3D, Nikon
111 Metrology). However, in the above methods there are some disadvantages: pre-determined
112 correction profiles do properly beam hardening curves, custom user-specified correction profiles
113 suffer from a difficulty in determining the optimum coefficients as they are only determined
114 from a single central slice; and custom auto-detected correction profiles require a mono-material
115 sample, which is generally not possible for geological samples. One of the post-reconstruction
116 linearization processes, is the method proposed by Jovanović et al. (2013), in which the beam
117 hardening correction is simultaneous to segmentation of the images. The procedure is based on
118 the calculation of beam hardening curves for each phase and as such it is time demanding.
119 Moreover, it is not applicable to samples in which discrimination between different phases is not
120 possible, for example in materials with a small grain size or in low-resolution scans.

121 In this study develop a new method for post-reconstruction beam hardening linearization. By
122 considering the limits related to the correction techniques described above, we develop a beam
123 hardening correction method that:
124   1. is suitable for near-cylindrical geological (multi-mineral) core samples,
125   2. does not require a priori knowledge of the sample properties,
126   3. works on samples with a heterogeneous spatial distribution of materials,
127   4. is applied post-reconstruction, hence works on any X-ray source and scanner
128   configuration,
129   5. is open source, customizable, and suitable to run on a standard desktop computer.
130
131 To this end, an open source ImageJ plug-in was created. Details of the correction methodology
132 employed by the plug-in are provided in Supporting Information. The plug-in is validated on a
133 range of natural and artificial geological samples. We then discuss the implications of beam

134 hardening correction on porosity measurement, multi-phase flow measurement and quantitative
135 analysis of geological samples.

136 **2 Materials and Equipment**

137 Four samples with cylindrical and quasi-cylindrical shapes and increasing structural complexity
138 have been scanned with μCT cone-beam scanner (custom Nikon® XT H X-Ray CT with 180 and
139 225 kV sources) in the University of Strathclyde Advanced Materials Research Laboratory. One
140 of the samples, a Berea Sandstone, has also been scanned with a General Electric Hi-Speed CT/i
141 at the Benson Lab, Stanford University. Scanner settings were chosen to maximise resolution
142 and image quality for each sample scan resulting in the use of different distances from the source
143 and detector, physical filters, values of X-ray energy, current, detector exposure, and even X-ray
144 source unit depending on the sample's physical properties. More details about the settings used
145 for each sample are included Table1.


146   2.1 Plastic rod
147 A grey Polyvinyl Chloride rod of 40mm of diameter was scanned to validate the plug-in on
148 homogeneous material.

149   2.2. Loose sand sample
150 A plastic cylinder was filled with coarse-grained sand pluviated from a constant distance and
151 frequently tapped to ensure uniform packing. The container had an external diameter of 60 mm
152 and an internal diameter of 50 mm.

153   2.3. Deformation band sample
154 A fine-grained core sample of the Navajo Sandstone Formation was collected at a depth of 59.74
155 m from a borehole (BH3) in the area of Big Hole Fault, Utah (Shipton, et al., 2002). The core,
156 measuring 60 mm in diameter and 178 mm in length, has 3-4 single anastomosing deformation
157 bands running through the sample. To allow air permeameter tests along the core length, this
158 sample had previously been slabbed creating a 20 to 29 mm wide flat edge (Fig.1) hence it was
159 no longer a perfect cylinder when scanned.

Gray value

100 pixels

0   65535
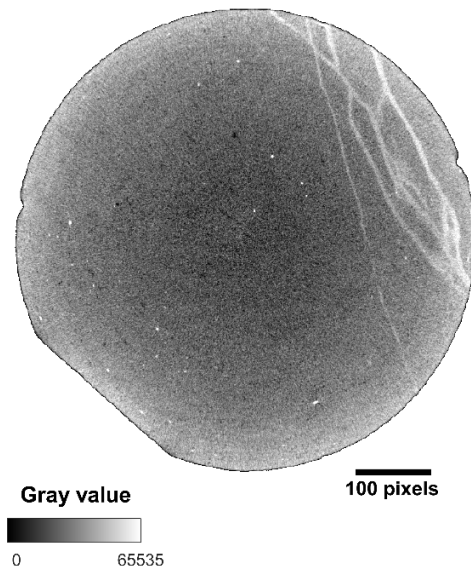
160

161   **Figure 1.** Un-corrected slice number 1024 of deformation band core sample. The original core
162   sample had been cut for permeameter tests, and the operation created a flat edge. Pixel size is
163   100 μm.

164   2.4. Deformation band network core sample
165   From the same borehole as the first sample a roughly cylindrical Navajo Sandstone core (BH3-1)
166   with length 96 mm and diameter of 60 mm, was collected at a depth of 60.44 m (Shipton et al.,
167   2002). The sample is characterised by a dense network of deformation bands.

168   2.5. Berea sandstone General Electric Hi-Speed CT/i
169   A homogeneous Berea Sandstone (sample dimensions 100 mm long, 50.8 mm diameter)
170   extracted from the Upper Devonian Berea sandstone formation in Ohio, USA, was scanned with
171   a General Electric medical scanner in both dry (pore space filled with air) and water-saturated
172   conditions. The scan was made before the microbially-induced calcite precipitation experiments
173   described in Minto et al., 2017a.

174   2.6. Berea sandstone μCT cone-beam scanner

175 A highly truncated internal scan of the Berea Sandstone core in section 2.5 above was made to
176 have a higher resolution of the upper part of the core, which was unaffected by calcite
177 precipitation (Minto, et al., 2017a). A truncated scan is one in which some of the sample lies
178 outside the field of view, hence, sample properties in region surrounding the scan are unknown.
179 Truncated internal scans made with a cone-beam CT do not normally result in a high quality
180 reconstruction, since they are prone to artefacts caused by X-ray attenuation in the unknown
181 region. This type of artefact presents in a similar manner to beam hardening.

Sample	Distance source object (mm)	Distance object detector (mm)	Energy (kV)	Current	Physical filter	Resolution
Plastic	168.43	505.36	140	86 μA	2 mm Al	49 μm
Loose sand	370.55	688.5	120	196 μA	None	70 μm
Single db	377	377	140	86 μA	0.25 mm Cu	100 μm
Db network	184	867	145	173 μA	1mm Cu	35 μm
Berea medical scan	630	469.31	120	200 mA	None	0.4883 mm
Berea Cone Beam	33.7	640	178	53 μA	1mm Cu	10 μm

182 **Table 1.** Table summarizing the settings used and resolutions obtained for each sample scanned.

183 **3 Beam hardening correction procedure**

184 In this section, we explain the theory underpinning the proposed beam hardening correction
185 procedure. The code, and a step-by-step operating procedure, are included in
186 http://dx.doi.org/10.15129/2fb54088-1187-48f2-832b-ef76cf5e7bc1.

187   3.1 *Radial profile* calculation
188 The code is suitable for core samples and roughly cylindrical shapes, or for samples contained
189 within a cylindrical core holder or other cylindrical container (for example in the case of the
190 loose material, see 2.2). For images obtained with a cone beam geometry scanner, we advise
191 avoiding correcting the slices at the very top and very bottom of the sample. These are affected
192 by geometric unsharpness (*penumbra*) and their attenuation values are not related to the actual
193 composition of the sample, but to geometric factors of the cone beam geometry. The quantity of
194 slices to not consider is variable and depends on the source-object, object-detector distances and
195 the focal spot size (Pauwels, et al., 2014).

196 As described above, beam hardening in cylindrical shapes produces alteration of the attenuation
197 values in relation to the distance from the centre. Consequently, it seems reasonable to propose a
198 correction based on a radial linearization beam hardening curve.

199 The beam hardening curve is calculated using the plug-in *Radial Profile Extended* (Carl, 2006).
200 The beam hardening curve, from here on termed the *radial profile* is a radial average of the
201 attenuation values as a function of the distance from the centre of the sample. The plug-in, in
202 fact, draws concentric circles (usually increasing the radius by 1 pixel) and calculates for each
203 circle the sum of the attenuation or intensity values divided by the number of the pixels included
204 in the circle. In this way, the radial profile is defined for each slice. For computational efficiency,
205 all the radial profile curves obtained (one for each slice once the top and bottom slices affected
206 by penumbra have been removed) are averaged and one single average radial profile (Fig.2) is
207 obtained. In this way, the following fitting of beam hardening curve is operated only once. Using
208 a single average radial profile also improves the correction process if there are some
209 heterogeneities in the sample, since it is not much affected by unusually high values, such as
210 those caused by the presence of deformation bands, bright grains, noise (Fig.2), or conversely by
211 low values related to fractures.

212 In some scans a trend may be observed in the average radial profile for each slice, moving
213 through the sample, due to poor positioning of the X-ray source. If this is the case, a single
214 average radial profile will be not representative of all the slices. To address this, a second version
215 of the code is provided, that corrects for beam hardening on a slice-by-slice basis following the
216 same procedure as that described below, but using the individual average radial profile for each
217 slice. This alternative code takes a long time to process, but in these circumstances, provides
218 more accurate results.
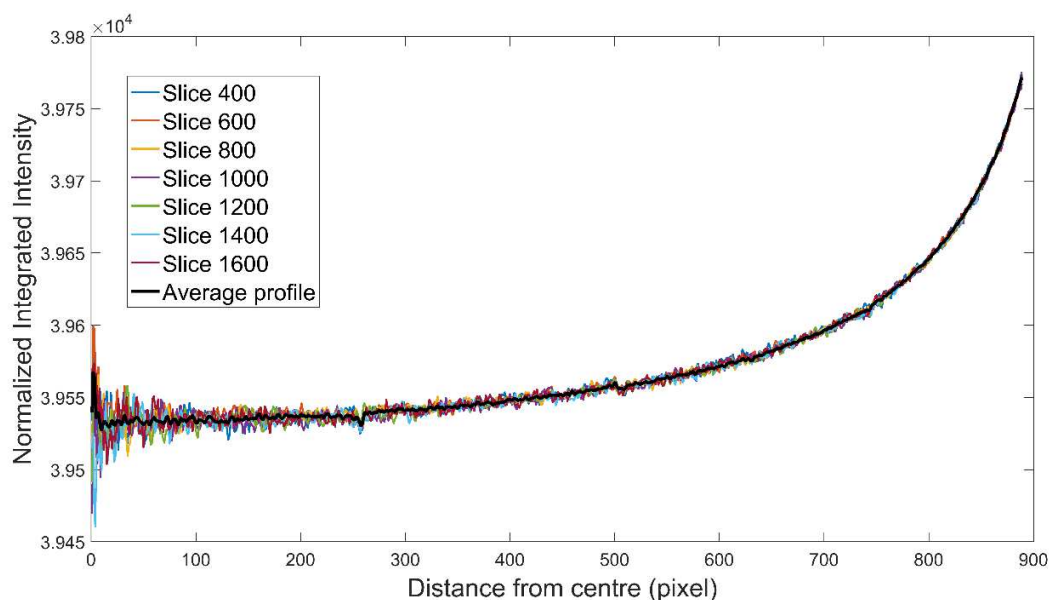
219
220 **Figure 2.** Radial profile of several slices of the Berea sandstone core sample CTCB and the
221 average radial profile (black) used for the curve fitting.

222   3.2 Curve fitting

223 To proceed to the beam hardening correction, we fit the average radial profile using two
224 equations: an exponential function with offset and an Inverse Rodbard relationship. The first is a
225 single-coefficient exponential model with a vertical offset *c*,
226

$$y = ae^{(-bx)} + c \qquad (2)$$

227 The second is a four-parameter logistic regression model (4PL):
228

$$y = c \left(\frac{(x-a)}{(d-x)}\right)^{\frac{1}{b}} \qquad (3)$$

229 The *a* and *d* coefficient are, respectively, the lower and upper asymptotes. The *b* coefficient
230 represents the steepness of the curve, and the *c* coefficient is the halfway point between *a* and *d*.
231
232 Figure 3 illustrates the best fit curves for both the Exponential model and the Inverse Rodbard
233 model for the average radial profile in Figure 2. The exponential function alone does not provide
234 an accurate correction because it is not able to accurately fit the steep section of the average
235 radial profile close to the edge of the sample (Fig.3). By contrast, the Inverse Rodbard provides a
236 good fit to the radial profile at the edge of the sample but is unable to fit to the shallow part of
237 the curve at the centre of the core (Fig.3).
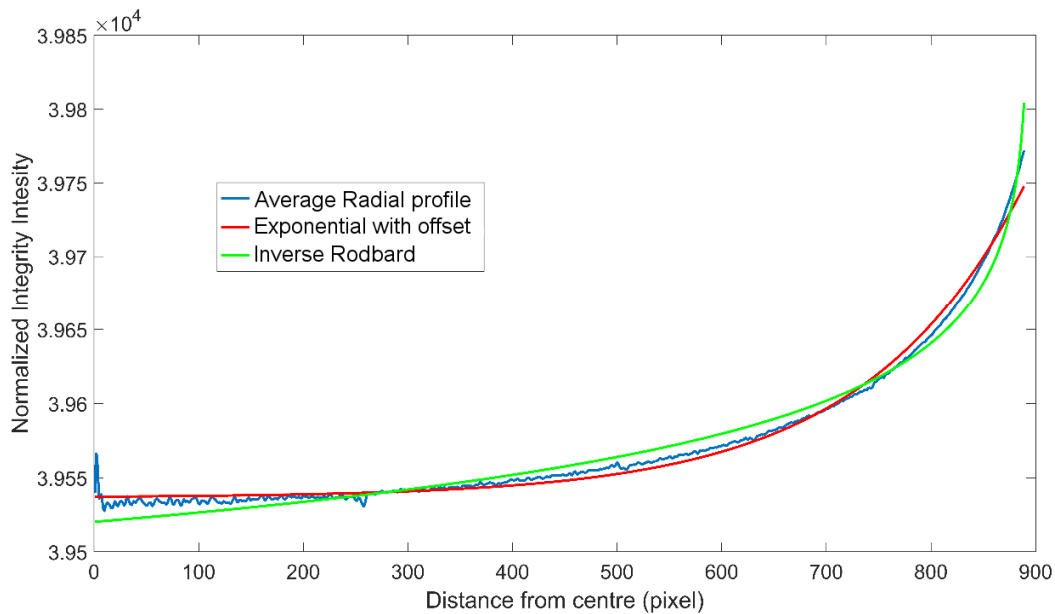
238
239 **Figure 3.** Curve fitting on the average radial profile (blue) of several slices of the Berea
240 sandstone core sample with both Exponential with offset function (red) and Inversion Rodbard
241 function (green).

242 Based on these considerations, we fit both the Exponential with offset and the Inverse Rodbard
243 equations to the inner and outer parts of the average radial profile respectively (Fig.4). The
244 curvature of each function is related to the maximum and minimum values of each of the two
245 fitted sections. Hence, to obtain a good fit it is important to define the boundary between the two
246 regions, termed the cut-off point (COP, Figure 4). Sensitivity tests were made to determine the
247 best value for the COP that minimised errors in the fit. This resulted in the COP being defined by
248

$$COP \approx \left(\frac{(max - m_{10})}{100} * 25 \right) + m_{10} \qquad (4)$$

249 where m_{10} is the mean value of the first 10% of the curve, to remove noise at the centre of the
250 image, and *max* is the maximum value of the average radial profile.

251 A small overlapping window between the two portions of the curves (Fig.4) is set during fitting
252 to ensure a smooth transition from one function to the next at the cut-off point (i.e. to remove any
253 kink).
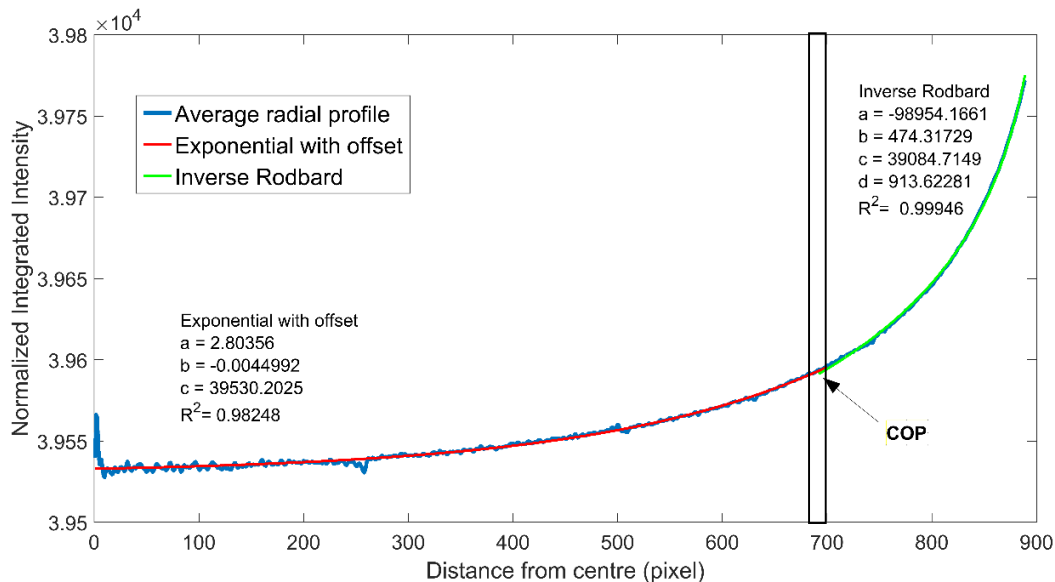
254
255 **Figure 4.** The average radial profile of Berea sandstone core sample is split in two for the curve
256 fitting with Exponential with Offset in the central part and with Inverse Rodbard in the outer
257 part. The black box is referred to as the overlapping window.

258 To facilitate the curve fitting and reduce the number of iterations taken to find a reasonable
259 solution for the fitting of the *Inverse Rodbard*, it is desirable to define initial guesses for the *a*, *b*,
260 *c*, and *d* coefficients in the equation. This is also serves to ensure that the iterative fitting
261 procedure converges. Considering that the *a* coefficient is the lower asymptote and usually has
262 negative values, we set its initial guess as 0. The *d* coefficient is the point at which the curve
263 reaches its maximum value; for this reason, we use an initial guess equal to the radius. For
264 investigating the behaviour of the *b* and *c* coefficients, the fitted values for samples 2.1, 2.2, 2.3,
265 2.4, and 2.6, plus two scans made with different X-ray calibration settings for both the plastic rod
266 and for sample 2.5 (Fig.5). The *b* and *c* coefficients follow respectively a Power law (Fig.5a)
267

$$y = 278245 \, x^{(-1.218)} \tag{5}$$

268   and an exponential law (Fig.5b)

269

$$y = 38641 \, e^{-0.0003x} \tag{6}$$

270

271   when plotted against the logarithm of the difference between the maximum and minimum values
272   of the section of the radial profile fitted by the Inverse Rodbard function.

273   For heterogeneous samples (loose sand and multiple deformation bands samples) the b
274   coefficient covers several orders of magnitude for the same range on the x-axis (Fig. 5a). For
275   these samples, using the full range of values on Figure 5a for the initial guess resulted in the
276   same solution. The initial guess for the value of c can be better constrained (Fig. 5b). For both
277   the b and c coefficients, changes to the calibration of the X-ray CT scanner led to significantly
278   different fitted values (old scans on Fig.5).

279   a)

280
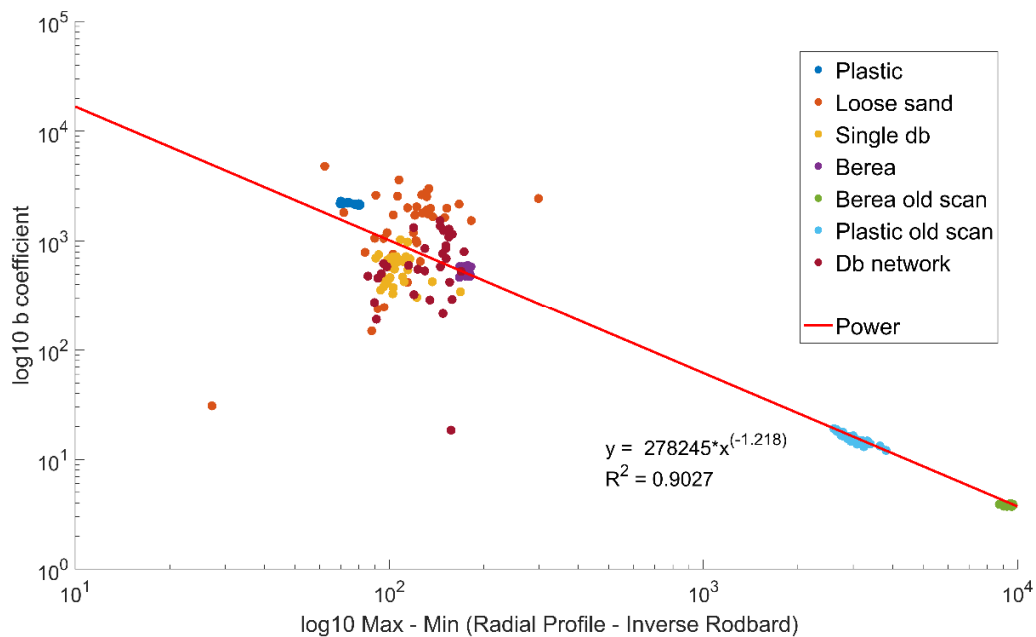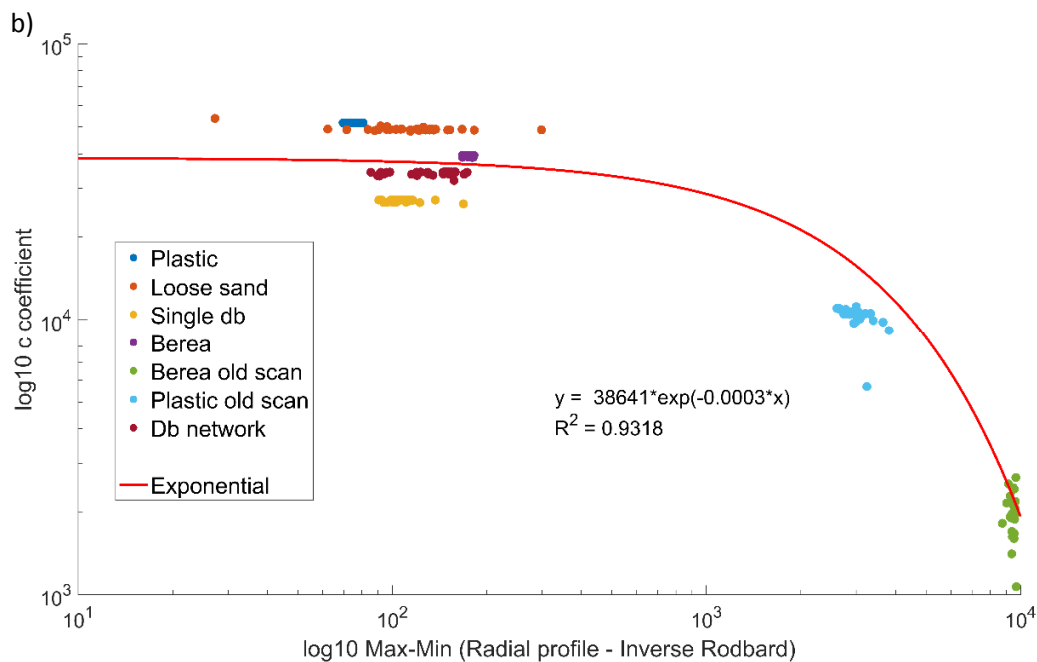
Figure 5. a) *b* coefficient values vs the difference between maximum and minimum value of the Radial profile interested by inverse Rodbard fitting. It follows a power law. b) *c* coefficient values vs the difference between maximum and minimum value of the Radial profile interested by Inverse Rodbard fitting. It follows an Exponential law.

Once the initial guesses have been defined, it is possible to fit the average profile and, using the calculated coefficients for each equation, *Exponential with offset* and *Inverse Rodbard*, to correct each pixel of the image.

4 Results

The plug-in was applied to all of the samples described in Section 2. In each case, the beam hardening artefact was significantly reduced, and the method did not produce any over-correction or blurring of the image.

4.1 Homogeneous sample

In this section we show the results for the plastic rod (Fig.6 a,b,c) and the loose sand material sample (Fig.6 d,e,f). The plastic rod was used for testing the reliability of the plug-in and to show that beam hardening occurs in a homogeneous, uniform material. Whereas, the loose sand sample whilst still being a homogeneous sample, contains multi-mineral components. Visual analysis of Figure 6 shows that an excellent correction has been achieved in each case.

a)

100 pixels

b)

100 pixels

c)

d)

100 pixels

e)

100 pixels

f)
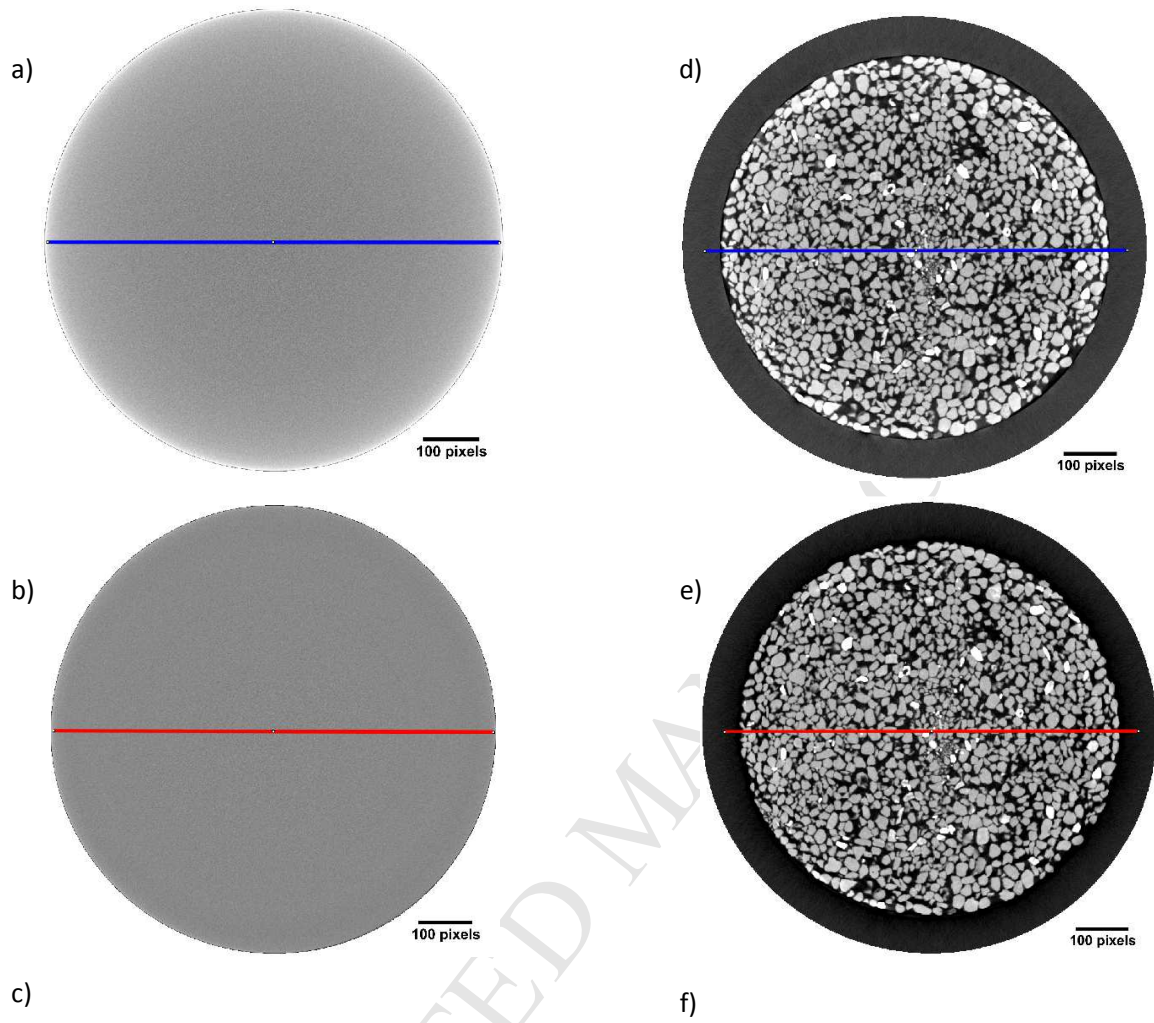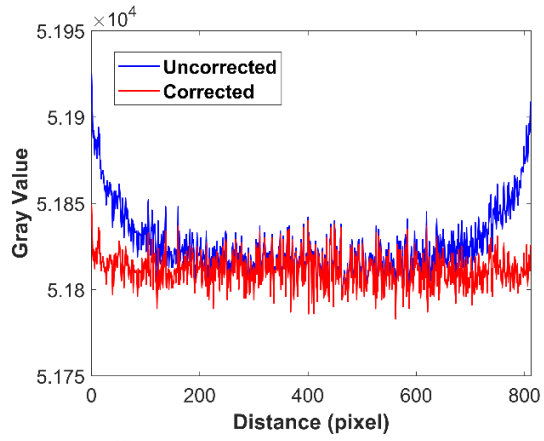
299
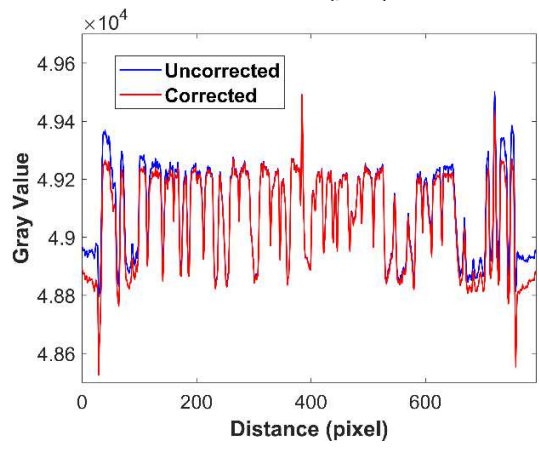
300

301 **Figure 6.** a) Slice number 1567 of Plastic rod un-corrected; b) slice number 1567 of Plastic rod
302 un-corrected corrected with the plug-in proposed; c) plot of attenuation values along the
303 selections of the un-corrected (blue) and corrected image (red); pixel size is 49 μm. d) Slice
304 number 1299 of Loose sand with outer ring sample un-corrected; e) slice number 1299 of Loose
305 sand with outer ring sample corrected with the plug-in proposed; f) plot of attenuation values
306 along the selections of the un-corrected (blue) and corrected image (red). Pixel size is 70 μm.

307　　　　4.2 Non-uniform shapes and heterogeneous samples
308 Figure 7 shows results of the correction applied to the deformation band core sample and the
309 deformation band network core sample. Both have near-cylindrical shapes and contain structural
310 heterogeneities in the form of deformation bands and/or fractures.

a)

d)

100 pixels

100 pixels

b)

e)

311

312
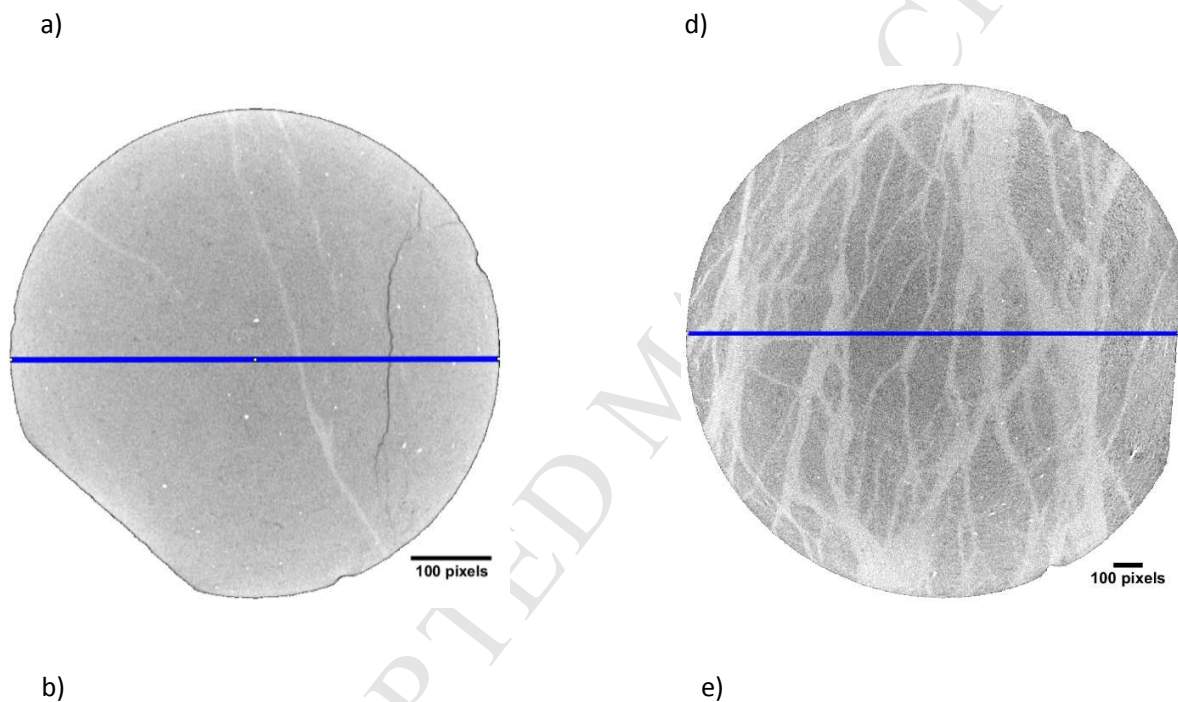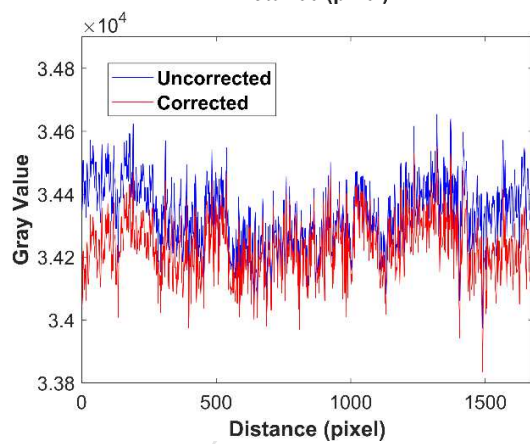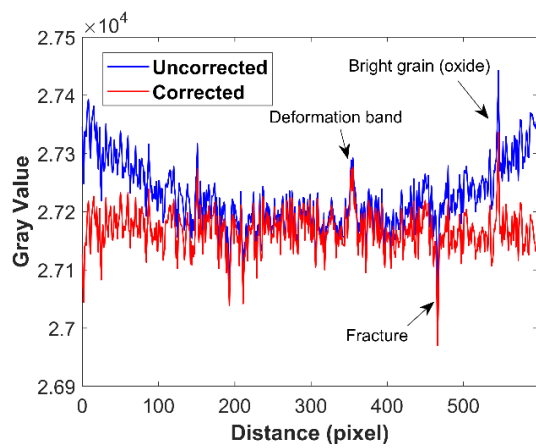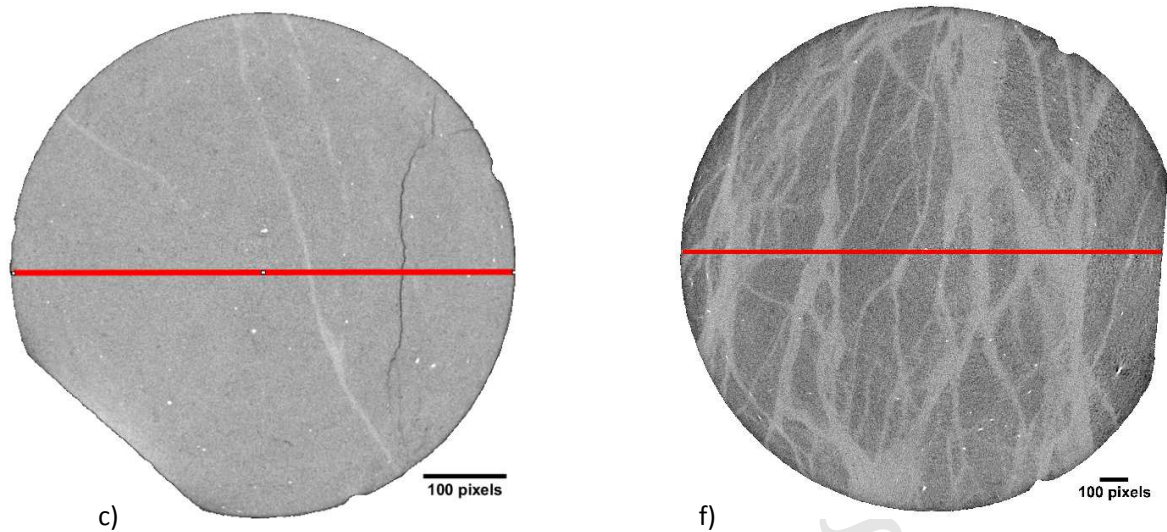
Figure 7. a) Slice number 1660 of sand sample un-corrected; b) slice number 1660 of sandstone with deformation bands core sample corrected with the plug-in proposed c) plot of attenuation values along the selections of the un-corrected (blue) and corrected image (red). In both profiles is possible to distinguish a positive spike related to the deformation band, a negative spike related to the fracture and another positive one due to the presence of oxides in the rock. Pixel

318   size is 100 μm. d) Slice number 1029 of multiple deformation bands core sample un-corrected; e)
319   slice number 1029 of multiple deformation bands core sample corrected with the plug-in
320   proposed; f) plot of attenuation values along the selections of the un-corrected (blue) and
321   corrected image (red). Pixel size is 35 μm.

322   For cores containing a slabbed edge, a second artefact, in addition to beam hardening is present.
323   This artefact is termed the exponential edge-gradient effect (EEGE) (Joseph & Spital, 1981) and
324   is a non-linear effect arising from the intersection of x-ray paths at corners, which is not
325   accounted for in filtered back-projection algorithms. Its effect results in a lowering of the
326   attenuation values at corners (Ketcham & Hanna, 2014) (Fig.8a). For this reason, the correction
327   was not able to fully correct the beam hardening close to the slabbed edge (Fig.8b) and we advise
328   avoiding quantitative measurements in this region.
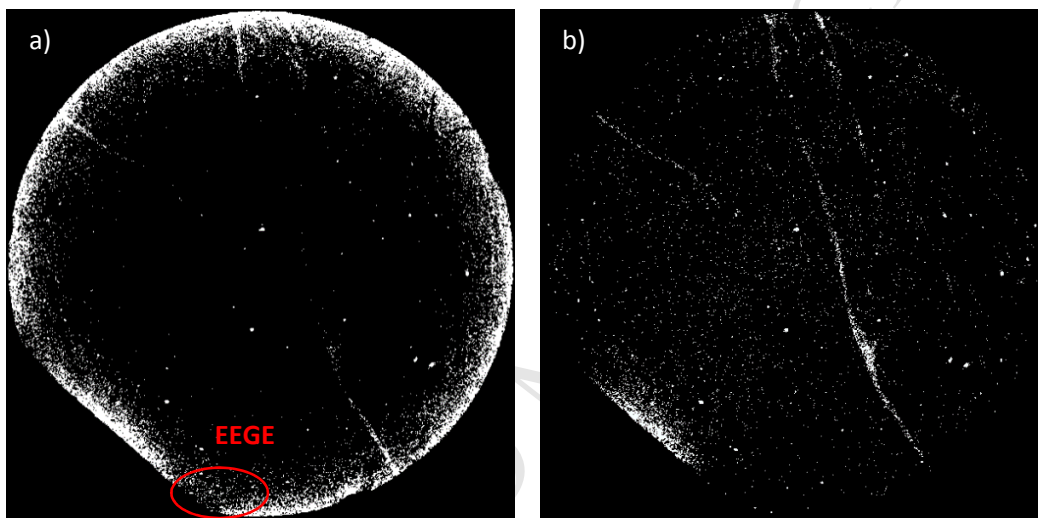
329

330   **Figure 8.** a) Segmented un-corrected image of sandstone with deformation bands core sample.
331   Beam hardening artefact is not a radial function for non-cylindrical shapes. Lower attenuation
332   values along the corner due to EEGE. b) Segmented corrected image of sandstone with
333   deformation bands core sample. The combined EEGE/beam hardening artefact is not corrected
334   along flat portion.

335   For the deformation band network sample, segmented images clearly show the beam hardening
336   artefact. Without the correction it is not possible to define the complete pattern of the
337   deformation bands (Fig.9a) since segmenting the portion of the deformation bands close to the
338   edge means that the central part of the bands disappears. With the correction applied, Fig. 9b, the
339   band network is clearly visible.
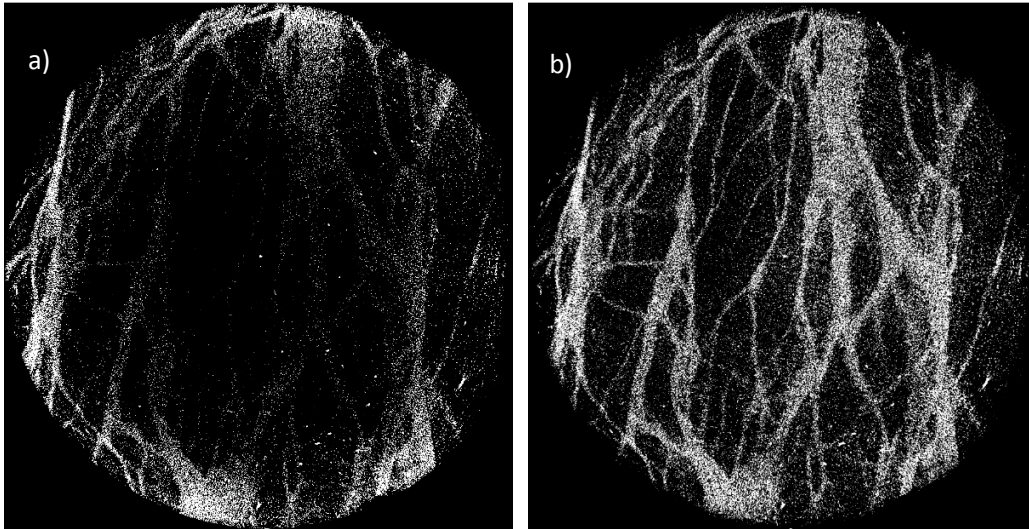
340

341 **Figure 9.** a) Segmented image of multiple deformation bands core sample un-corrected. Without
342 correction it is not possible to recognize completely the deformation bands. b) Segmented image
343 of multiple deformation bands corrected. All the deformation bands are shown.
344

345   4.3 Berea sandstone core sample with the medical scan
346 We also applied the correction plug-in to the medically scanned Berea sandstone sample (section
347 2.5). Figure 10 shows how the code can also remove the beam hardening effect in this lower
348 resolution medical CT scanner dataset. For this specific case, some pixels next to the outer metal
349 ring have been not considered for the correction and analysis. This is because they are not pixels
350 of the sample, but due to the low resolution represent both the core sample and the outer metal
351 ring. Using such pixels would produce a beam hardening curve that is steeper and not truly
352 representative of the core sample, which will then, in turn, not be properly corrected.

353
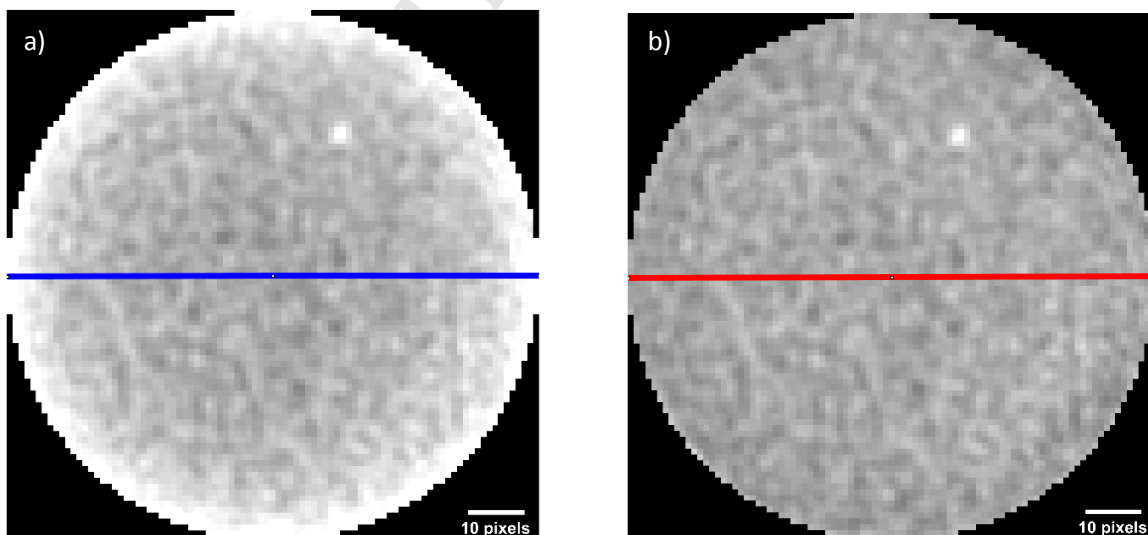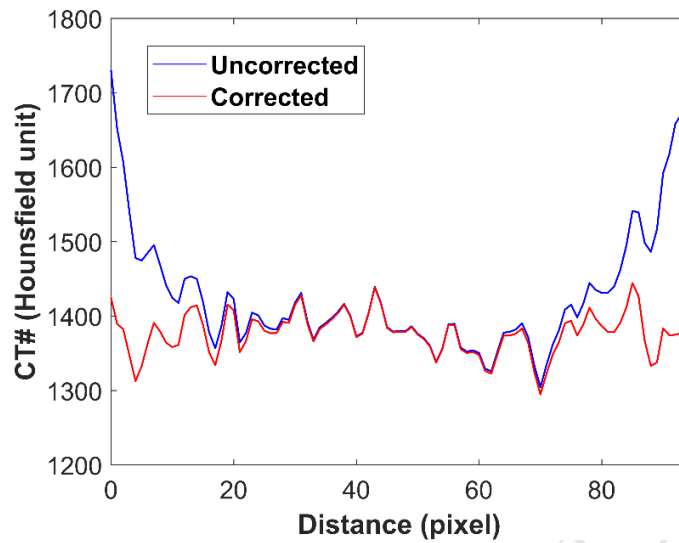
Figure 10. a) Slice number 59 of water-saturated Berea sandstone core sample un-corrected. This dataset has been acquired with a medical scan; b) slice number 59 of Berea sandstone core sample corrected with the plug-in; c) plot of attenuation values along the selections of the un-corrected (blue) and corrected image (red). Pixel size is 0.4883 mm.

4.4 Berea sandstone core sample internal scan CBCT

Finally, Figure 11 shows the results of the beam hardening correction plug-in applied to the truncated scan of the Berea Sandstone core sample (section 2.6). Once again, the correction is very successful and the scan artefacts have been removed.

c)
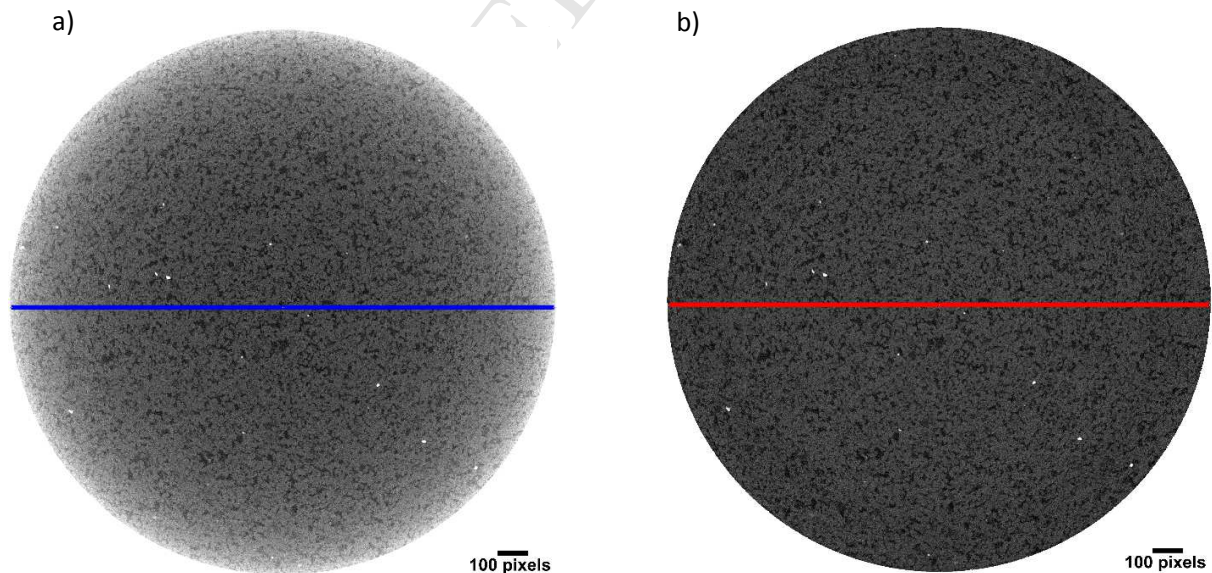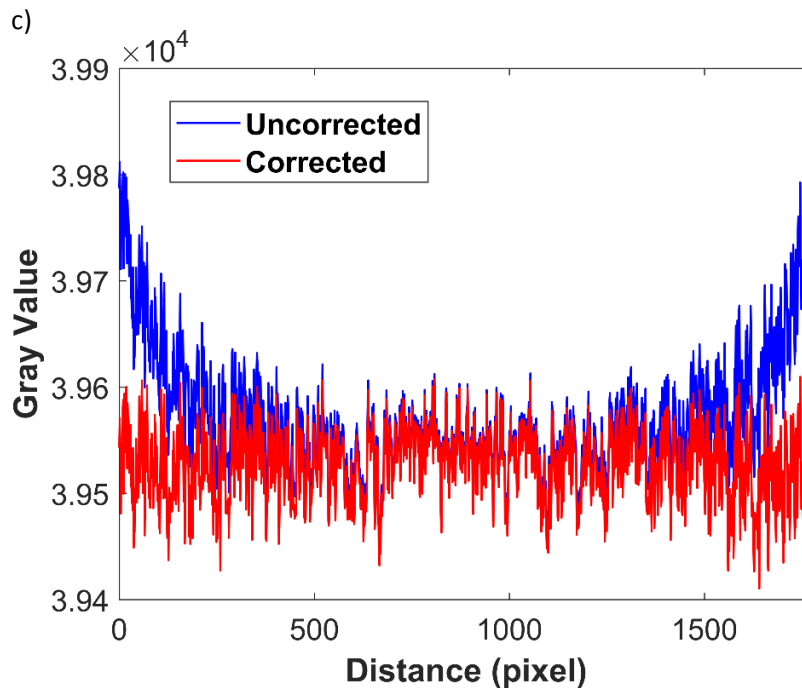
Figure 11. a) Slice number 690 of Berea sandstone core sample un-corrected; b) slice number 690 of Berea sandstone core sample corrected with the plug-in; c) plot of attenuation values along the selections of the un-corrected (blue) and corrected image (red). Pixel size is 10 μm.

5   Determination of core scale petrophysical properties

5.1 Determination of core scale porosity
Determination of porosity through X-ray CT can be achieved following two main methods. The first one requires one single scan with enough resolution to distinguish void and solid phases. The second method instead consists of using two sets of scan images, one in which the sample is dry and the other in which the sample is fully saturated with water.


5.1.1 Segmentation-based method
The segmentation-based method for porosity calculation is common, since it only requires a single scan and, therefore, conserve times and money. To be achievable, the resolution of the scan must be high enough to threshold the images and separate the voids from the grains. To check the improvement provided by the plug-in porosity calculation using segmentation, we consider the internal scan of the Berea sandstone core sample. We use an internal scan, since for this method, we require an extremely high resolution image. Using a single slice, 2D images of porosity were created using a standard thresholding approach to convert the grey scaled image into a binary image (i.e. pore/not pore). The threshold values are selected such that voids and grains have values of 1 and 0 respectively. Finally, porosity is obtained by calculating the proportion of pixels valued at 1 or 0 in the shape described by the sample.

We compared results derived using the plug in with those taken straight from the auto-detected correction software supplied with the instrument, CT pro 3D. Even when we used the *strong*

386 correction in the software, it was not able to remove the cupping effect. As explained in the
387 Introduction, in the CT pro 3D software it is possible to customize the correction profiles and
388 choose different coefficients to those proposed in the *strong* correction, although there is no
389 methodology for their selection. For the uncorrected sample, a porosity of 7.23% is obtained
390 (Fig.12a); the porosity calculated for the slice using the *strong* correction option in the Nikon
391 software is 14.24% (Fig.12b); and the porosity calculated with the new beam hardening
392 correction is 20.54% (Fig.12c).

393 Petroleum reservoirs are mostly sandstones, underestimates in porosity of ~13% with no
394 correction and ~6% using the commercially supplied software, would be highly significant and
395 would lead to incorrect assessments of reservoir quality. In fact, 7.23% porosity is outside the
396 usual range for a homogeneous sandstone and even a difference in porosity estimate from 20.5%
397 to 14.24% would result in a downgrading of reservoir quality from good to fair. It is clear the
398 correction plug-in has a significant effect on the estimate of porosity, so it is important to
399 determine accuracy of these porosity estimates.

a)

Φ=7.23%

b)

Φ=14.24%

c)

Φ=20.54%

400
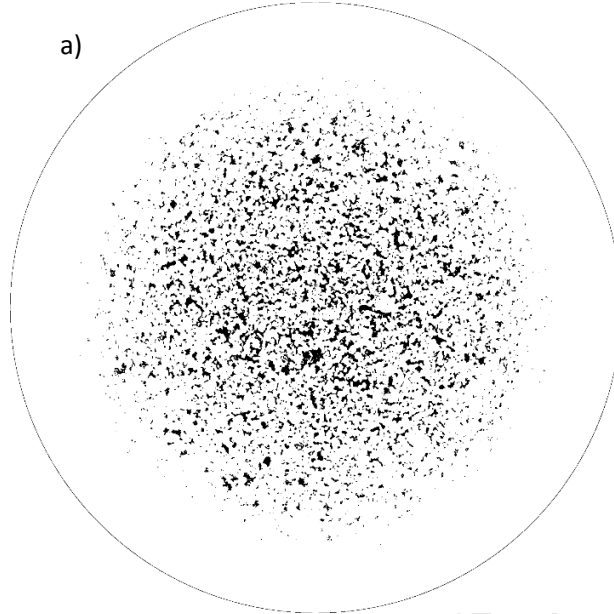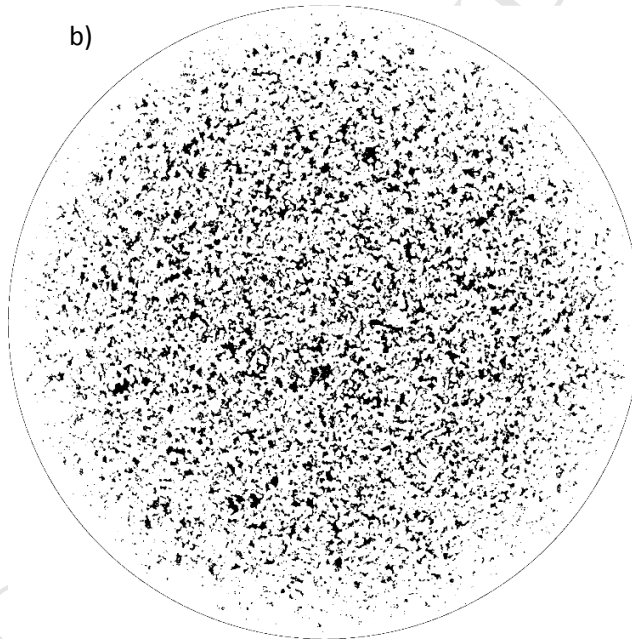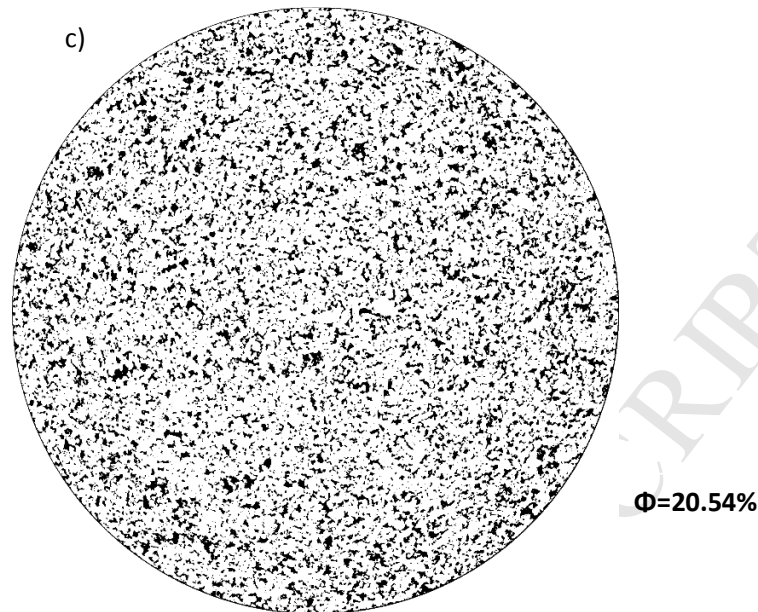
Figure 12. a) Image thresholding of slice 690 of Berea sandstone core sample un-corrected: calculated porosity is equal to 7.23%; b) Image thresholding of slice 690 of Berea sandstone core sample with strong correction of Nikon software: calculated porosity is equal to 14.24%; c) Image thresholding of slice 690 of Berea sandstone core sample with beam hardening correction: calculated porosity is equal to 20.54%.

5.1.2. Saturated and dry scans method

The saturated and dry scan method for determining porosity is commonly more accurate than the single-scan method, since it uses the 'difference' between the wet and dry scans. As a consequence, if the errors incurred during reconstruction are the same in the wet and dry images, then taking one image form the other removes them. Using this method, the porosity is calculated by (Krevor, et al., 2012)

$$\Phi = \frac{CT_{watersaturated} - CT_{dry}}{I_{water} - I_{air}} \tag{7},$$

where the denominator is defined as the difference between the Hounsfield units of the air (-1000) and the water (0). The method also has the advantage that it can be used on low resolution scan images, in which each voxel contains both pores and grains.
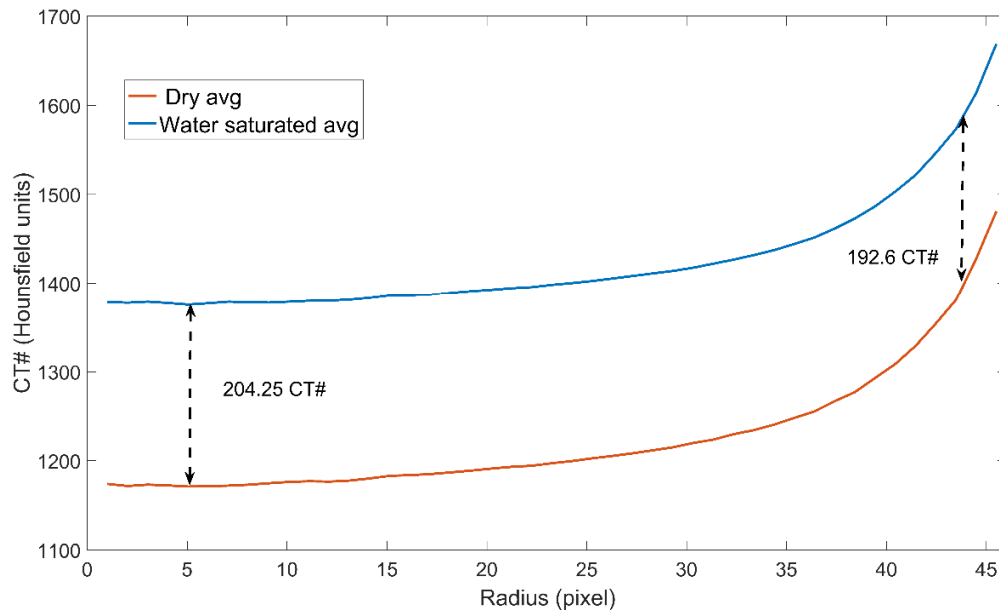
416
417 **Figure 13.** Difference between beam hardening curves of the water saturated and dry datasets.
418 Each curve has been obtained by averaging all the slices of the corresponding dataset and
419 calculating the radial profile.

420 The wet and dry method was used to obtain a porosity estimate for the Berea sandstone core,
421 acquired with the medical scanner (an internal cylindrical high resolution scan of the same core
422 was used for the single scan method above). Figure 13 shows radial profiles for the dry and
423 water saturated images, both of which are clearly affected by beam hardening. From visual
424 analysis, whilst the beam hardening effect in the two scans is similar, they have slightly different
425 curve shapes. This difference in curve shape means that the beam hardening effect does not
426 entirely disappear when subtracting the two datasets. As a result, the un-corrected porosity
427 estimate is characterized by a decrease in porosity toward the radial edge of the slice (Fig.14).
428 Since Berea sandstone is known to be very homogeneous, this trend can be attributed to the
429 different shapes of the beam hardening curves.
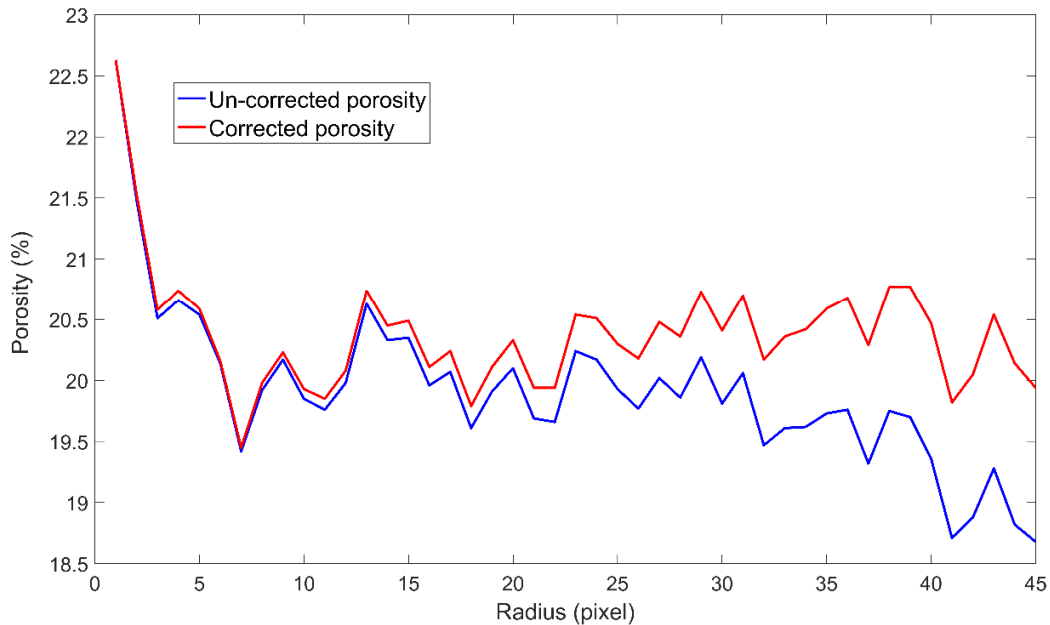
430
431 **Figure 14.** Radial profile of both un-corrected and corrected porosity of slice 59. The un-
432 corrected porosity decreases along the edges of the sample.

433 Both images, dry and water-saturated, were corrected with the proposed plug-in and the porosity
434 was then re-calculated. The core average total porosity was calculated in each case, resulting
435 values of 20.5% and 19.82% for the corrected and un-corrected images respectively (Fig.15).
436 The absolute error on porosity for both measurements is ±1.36% (of the calculated total porosity)
437 using the method proposed by Pini et al., (2012). It is clear from the Figure 14, that the two
438 porosity trends are divergent at the end of the sample: the porosity calculated using un-corrected
439 datasets decreases at the edge of the core, which is not justified by any specific compositional of
440 structural feature. Considering that this trend is present in all the slices of the core, the average
441 slice porosity of the un-corrected dataset is lower than the corrected one.

442
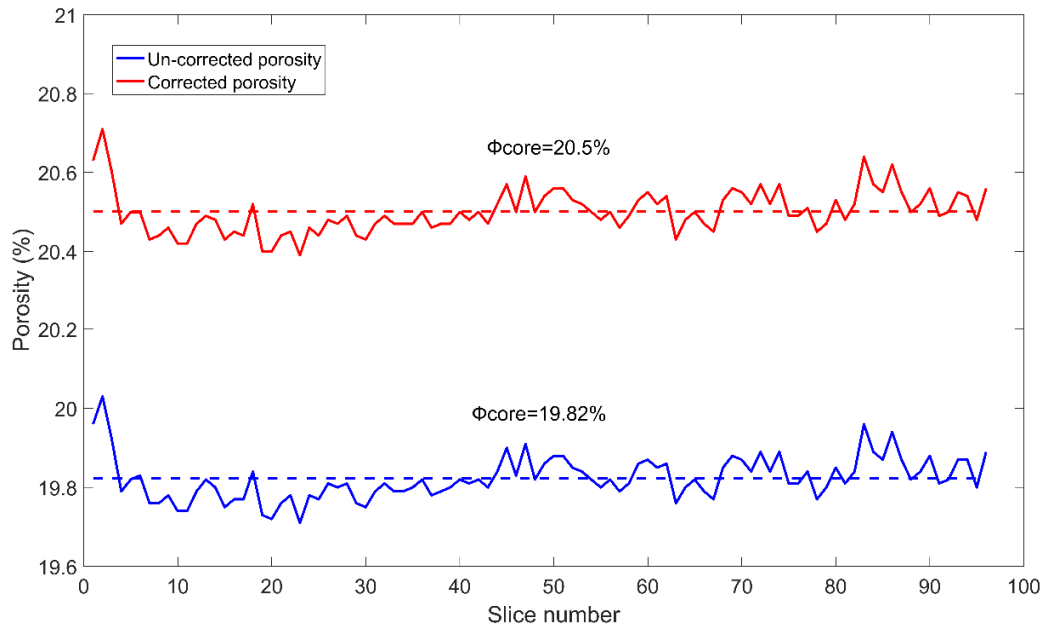
443
444 **Figure 15.** Average of un-corrected and corrected porosity for each slice (solid line) and the un-
445 corrected and corrected core average porosity (dashed line).

446   5.2 Determination of core scale permeability

447 Using CT data, pore-scale flow modelling can be used as a method of estimating the core-scale
448 permeability (~ 200 mD for host rock, ~ 1 mD for deformation bands). For example, using the
449 CT scan for the multiple deformation band core (Fig.16, left), each voxel is defined as either host
450 rock or deformation band (Fig.16, middle). The Navier-Stokes equations, with added Darcy-
451 Brinkman losses due to porous resistance (Minto, et al., 2017b), can then be solved numerically
452 to simulate 3D flow paths within the core (Fig.16, right). The modelled pressure drop across the
453 core for a simulation with a constant flow rate, can be used to calculate the core-average
454 permeability.
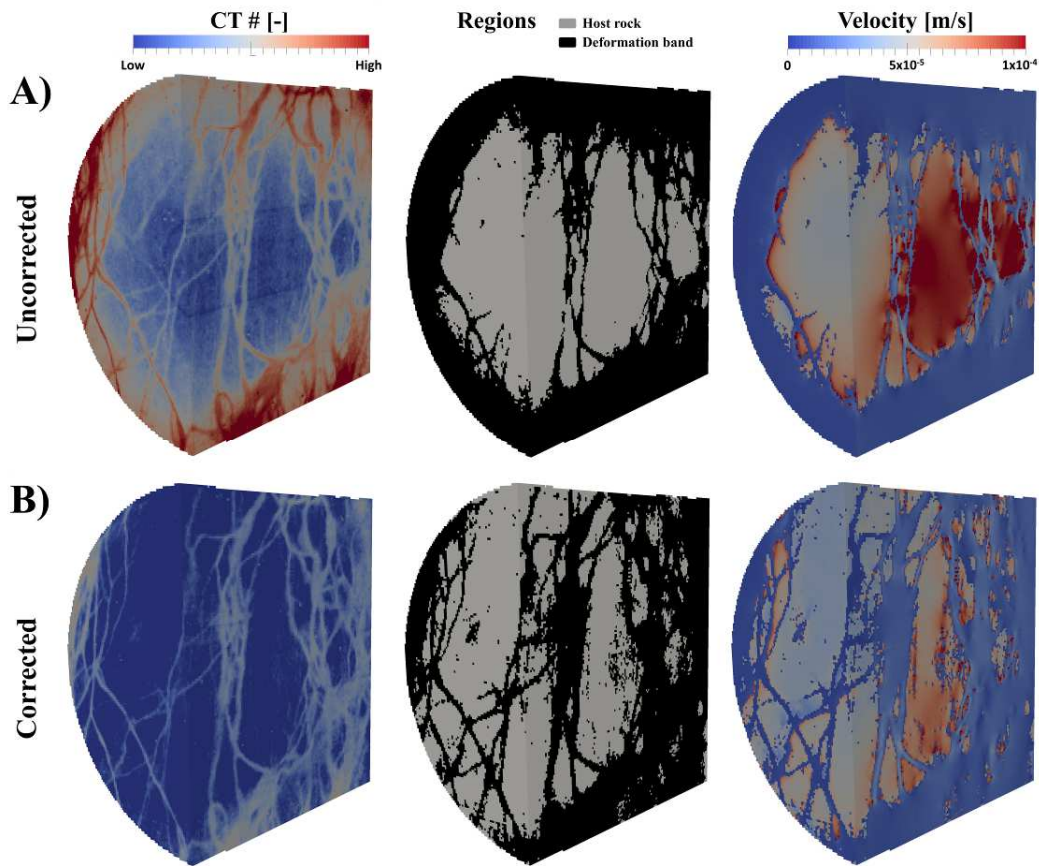
Figure 16. From left to right: X-ray attenuation value, binary segmented image, and calculated velocity distribution for A) the original uncorrected scan data and B) the same scan data after beam hardening correction. Core average permeability was calculated as 12.2 mDarcy for the uncorrected data and 6.47 mDarcy for the corrected model. Cores cut in half to visualise internal properties.

In the uncorrected dataset (Figure 16A), the deformation bands are underrepresented in the centre of the core and over represented at the edges. This creates an unrealistically high permeability central channel, through which most of the flow is focused, and leads to a bulk permeability estimate of 12.2 mD. Whereas, in the corrected dataset, the deformation bands are well represented throughout the core, resulting in a more uniform flow distribution and a bulk permeability estimate of 6.47 mD. The error in the spatial representation of deformation bands in the uncorrected core will also have implications for estimates of other petrophysical properties, in particular relative permeability and capillary entry values, both of which are key to understanding reservoir performance for CO_2 enhanced oil recovery, CO_2 trapping and long-term CO_2 storage.

6 Conclusion

In this study, we present a new technique for beam hardening correction. The method is completely automatic and independent of the sample material, the material heterogeneity, scanner resolution, and the scanner settings. The method is presented through development of an

475 open source plug-in running on ImageJ. The correction has been applied on both homogeneous
476 and heterogeneous cylindrical and near-cylindrical geological samples, and provides excellent
477 results in all cases. We show that application of the correction leads to significant differences in
478 the estimates of porosity and permeability. Further, unlike other beam hardening correction
479 methods, our plug-in can be used to correct for cupping errors in truncated internal scans. This is
480 highly valuable, since truncated scans provide small volume, high resolution data, without the
481 need for sample destruction.

482 **Computer Code Availability**
483 The name of the code is "Automated high accuracy, rapid beam hardening correction in X-Ray
484 Computed Tomography of multi-mineral, heterogeneous core samples". The developer of this
485 code is Carla Romano. James M. Minto is editor of the code; both Zoe K. Shipton and Rebecca J.
486 Lunn are supervisors of this work. Contact email is carla.romano@strath.ac.uk; telephone
487 number is +447460739755. The code is available to download at
488 http://dx.doi.org/10.15129/2fb54088-1187-48f2-832b-ef76cf5e7bc1, since 08th April 2018. There are
489 no hardware requirements. The code has been tested on Windows Vista 128GB of RAM
490 computer, on Windows 7 8GB of RAM computer on Windows 10 8GB of RAM computer and
491 also on works for Linux operating system. The code runs in Fiji - ImageJ software, it is written in
492 IJ1 language and its size is 16 KB. Workflow is included in "Step by step procedure" file. Two
493 versions of the code are provided. Please use the
494 "BeamHardening_Correction_plugin_NOaverage_profile" ijm file, if there is a gradient in
495 average gray values from top to bottom of your sample.
496 Software Requirements: - ImageJ/FIJI. Download available at https://imagej.net/Fiji/Downloads
497 - Radial Profile Extended plug-in (Carl P., 2006). Download available at
498 https://imagej.nih.gov/ij/plugins/radial-profile-ext.html

499 **References**
500 Biguri, A., Dosanjh, M., Hancock, S. & Soleimani, M., 2016. TIGRE: a MATLAB-GPU toolbox
501   for CBCT image reconstruction. *Biomedical Physics and Engineering Express,* 2(5).

502 Carl, P., 2006. *Radial Profile Extended.* [Online]
503   Available at: https://imagej.nih.gov/ij/plugins/radial-profile-ext.html
504   [Accessed 6 4 2018].

505 Cnudde, V. & Boone, M. N., 2013. High-resolution X-ray computed tomography in geosciences:
506   A review of the current technology and applications. *Earth-Science Reviews,* Volume 123,
507   pp. 1-17.

508 Feldkamp, L. A., Davis, L. C. & Kress, J. W., 1984. Practical cone-beam algorithm. *Journal of
509   the Optical Society of America A,* 1(6), pp. 612-619.

510 Gilbert, P., 1972. Iterative methods for the three-dimensional reconstruction of an object from
511   projections.. *Journal of theoretical biology,* 36(1), pp. 105-117.

512 Jennings, R. J., 1988. A method for comparing beam□hardening filter materials for diagnostic
513   radiology. *Medical physics,* 15(4), pp. 588-599.

514 Joseph, P. M. & Spital, R. D., 1981. he exponential edge-gradient effect in x-ray computed
515   tomography. *Physics in medicine and biology,* 26(3), p. 473.

516 Jovanović, Z., Khan, F., Enzmann, F. & Kersten, M., 2013. Simultaneous segmentation and
517   beam-hardening correction in computed microtomography of rock cores. *Computers and*
518   *Geosciences,* Volume 56, pp. 142-150.

519 Kachelrieß, M., Sourbelle, K. & Kalender, W. A., 2006. mpirical cupping correction: A first□
520   order raw data precorrection for cone□beam computed tomography. *Medical physics,*
521   33(5), pp. 1269-1274.

522 Ketcham, R. A. & Hanna, R. D., 2014. Beam hardening correction for X-ray computed
523   tomography of heterogeneous natural materials. *Computers & geosciences,* Volume 67, pp.
524   49-61.

525 Krevor, S., Pini, R., Zuo, L. & Benson, S. M., 2012. Relative permeability and trapping of CO2
526   and water in sandstone rocks at reservoir conditions. *Water Resources Research,* 48(2).

527 Kruth, J. P. et al., 2011. Computed tomography for dimensional metrology. *CIRP Annals-*
528   *Manufacturing Technology,* 60(2), pp. 821-842.

529 Lager, A. et al., 2008. Low salinity oil recovery-an experimental investigation1. *Petrophysics,*
530   49(1).

531 Lechuga, L. & Weidlich, G. A., 2016. Cone Beam CT vs. Fan Beam CT: A Comparison of
532   Image Quality and Dose Delivered Between Two Differing CT Imaging Modalities.
533   *Cureus,* 8(9).

534 Minto, J. M., Hingerl, F., Benson, S. M. & Lunn, R. J., 2017a. X-ray CT and multiphase flow
535   characterization of a "bio-grouted" sandstone core: the effect of dissolution on seal
536   longevity. *Internal Journal of Greenhouse Gas Control,* Volume 64, p. 152–162.

537 Minto, J. M. et al., 2017b. "Microbial Mortar"- restoration of degraded marble structures with
538   microbially induced carbonate precipitation. *Manuscript submitted for publication..*

539 Mooney, S. J., 2002. Three□dimensional visualization and quantification of soil macroporosity
540   and water flow patterns using computed tomography. *Soil Use and Management,* 18(2), pp.
541   142-151..

542 Mooney, S. J., Pridmore, T. P. & Helliwell, J. B., 2012. eveloping X-ray computed tomography
543   to non-invasively image 3-D root systems architecture in soil. *Plant and soil,* 352(1-2), pp.
544   1-22.

545 Pauwels, R., Araki, K., Siewerdsen, J. H. & Thongvigitmanee, S. S., 2014. Technical aspects of
546   dental CBCT: State of the art. *Dentomaxillofacial Radiology,* 44(1).

547 Perrin, J. C. et al., 2009. Core-scale experimental study of relative permeability properties of
548   CO_2 and brine in reservoir rocks. *Energy Procedia,* 1(1), pp. 3515-3522.

549 Pini, R., Krevor, S. C. & Benson, S. M., 2012. Capillary pressure and heterogeneity for the
550   CO_2/water system in sandstone rocks at reservoir conditions. *Advances in Water*
551   *Resources,* Volume 38, pp. 48-59.

552 Ritschl, L., Bergner, F., Fleischmann, C. & Kachelrieß, M., 2010. Water calibration for CT
553   scanners with tube voltage modulation. *Physics in medicine and biology,* 55(14), p. 4107.

554 Shipton, Z. K. et al., 2002. Structural heterogeneity and permeability in faulted eolian sandstone:
555   implications for subsurface modelling of faults. *American Association of Petroleum*
556   *Geologists Bulletin,* Volume 86, pp. 863-883.

557 Van Geet, M., Swennen, R. & Wevers, M., 2000. Quantitative analysis of reservoir rocks by
558   microfocus X-ray computerised tomography. *Sedimentary Geology,* 132(1), pp. 25-36.

559 Wellington, S. L. & Vinegar, H. J., 1987. X-ray computerized tomography. *Journal of Petroleum*
560   *Technology,* 39(08), pp. 885-898.

Highlights

- We introduce a new and automatic method for correcting CT beam hardening artefact
- The method is implemented in an open source code running in ImageJ and it is suitable for expert and non-expert alike.
- The method has been tested on homogeneous and heterogeneous rock samples with cylindrical and near-cylindrical shapes
- We show how our method improves porosity and permeability measurements.